ALMA continuum observations of the protoplanetary disk AS 209

Evidence of multiple gaps opened by a single planet⋆

D. Fedele[1], M. Tazzari[2], R. Booth[2], L. Testi[3], C. J. Clarke[2], I. Pascucci[4], A. Kospal[5], D. Semenov[6],
S. Bruderer[7], Th. Henning[6], and R. Teague[6]

[1] INAF–Osservatorio Astrofisico di Arcetri, Largo E. Fermi 5, 50125 Firenze, Italy
[2] Institute of Astronomy, University of Cambridge, Madingley Road, Cambridge CB3 0HA, UK
[3] European Southern Observatory, Karl-Schwarzschild-Strasse 2, 85748 Garching bei Muenchen, Germany
[4] Lunar and Planetary Laboratory, The University of Arizona, Tucson, AZ 85721, USA
[5] Konkoly Observatory, Research Centre for Astronomy and Earth Sciences, Hungarian Academy of Sciences,
   Konkoly-Thege Miklós út 15-17, 1121 Budapest, Hungary
[6] Max Planck Institute for Astronomy, Königstuhl 17, 69117 Heidelberg, Germany
[7] Max Planck Institut für Extraterrestrische Physik, Giessenbachstrasse 1, 85748 Garching, Germany

ABSTRACT

This paper presents new high angular resolution ALMA 1.3 mm dust continuum observations of the protoplanetary system AS 209 in the Ophiuchus star forming region. The dust continuum emission is characterized by a main central core and two prominent rings at $r = 75$ au and $r = 130$ au intervaled by two gaps at $r = 62$ au and $r = 103$ au. The two gaps have different widths and depths, with the inner one being narrower and shallower. We determined the surface density of the millimeter dust grains using the 3D radiative transfer disk code DALI. According to our fiducial model the inner gap is partially filled with millimeter grains while the outer gap is largely devoid of dust. The inferred surface density is compared to 3D hydrodynamical simulations (FARGO-3D) of planet-disk interaction. The outer dust gap is consistent with the presence of a giant planet ($M_{\rm planet} \sim 0.7\ M_{\rm Saturn}$); the planet is responsible for the gap opening and for the pile-up of dust at the outer edge of the planet orbit. The simulations also show that the same planet could be the origin of the inner gap at $r = 62$ au. The relative position of the two dust gaps is close to the 2:1 resonance and we have investigated the possibility of a second planet inside the inner gap. The resulting surface density (including location, width and depth of the two dust gaps) are in agreement with the observations. The properties of the inner gap pose a strong constraint to the mass of the inner planet ($M_{\rm planet} < 0.1\ M_{\rm J}$). In both scenarios (single or pair of planets), the hydrodynamical simulations suggest a very low disk viscosity ($\alpha < 10^{-4}$). Given the young age of the system (0.5–1 Myr), this result implies that the formation of giant planets occurs on a timescale of $\lesssim$1 Myr.

**Key words.** protoplanetary disks – planet-disk interactions

1. Introduction

Axisymmetric gaps and rings such as those seen in the protoplanetary disks around HL Tau, TW Hya, HD 163296, HD 169142, AA Tau (e.g., ALMA Partnership et al. 2015; Andrews et al. 2016; Isella et al. 2016; Fedele et al. 2017; Loomis et al. 2017) can now regularly be unveiled by the extremely high resolution available with ALMA. The formation of gaps and rings in disks can be due to several mechanisms such as: planet formation (e.g., Papaloizou & Lin 1984); magneto-rotational instability (Flock et al. 2015); condensation fronts (Zhang et al. 2015); dust sintering (Okuzumi et al. 2016); photoevaporation (Ercolano et al. 2017).

The rings observed by ALMA show that the millimeter dust grains are radially confined regions in which inward radial migration is slowed down or stopped and so may be key to explaining the retention of large grains in disks on long (2–3 Myr) timescales (irrespective of the mechanism producing such "dust traps"). In addition, dust traps provide the ideal

environment in which to observationally constrain models of grain growth because – in contrast to other regions of the disk – they are regions in which radial drift is relatively unimportant, allowing dust to grow in situ (Pinilla et al. 2012). Given a measure of the local dust density, the timescale for dust growth to a given size is readily obtained from grain growth models (e.g., Birnstiel et al. 2012). Empirical measurement of the maximum grain size in traps would thus provide the cleanest test of the various assumptions (sticking probability, turbulent velocity, fragmentation threshold) that enter these models.

This paper presents new ALMA 1.3 mm continuum observations of the T Tauri disk AS 209 where axisymmetric gaps and rings are detected. AS 209 ($M_\star = 0.9\ M_\odot$, spectral type K5, $L_\star = 1.5\ L_\odot$, Tazzari et al. 2016) is part of the young (age ∼ 0.5–1.0 Myr; Natta et al. 2006) Ophiuchus star forming region at a distance of 126 pc from the Sun (Gaia Collaboration 2016). Multi-frequency continuum observations revealed optically thin emission at millimeter wavelengths beyond a few 10 s of au from the star (Pérez et al. 2012; Tazzari et al. 2016). Huang et al. (2016) found evidence of an extended gas emission ($C^{18}O$) speculating that it is due to external CO desorption in the outer disk. Interestingly, Huang et al. (2017) noticed the presence of a dark lane in the dust 1.1 mm continuum emission.
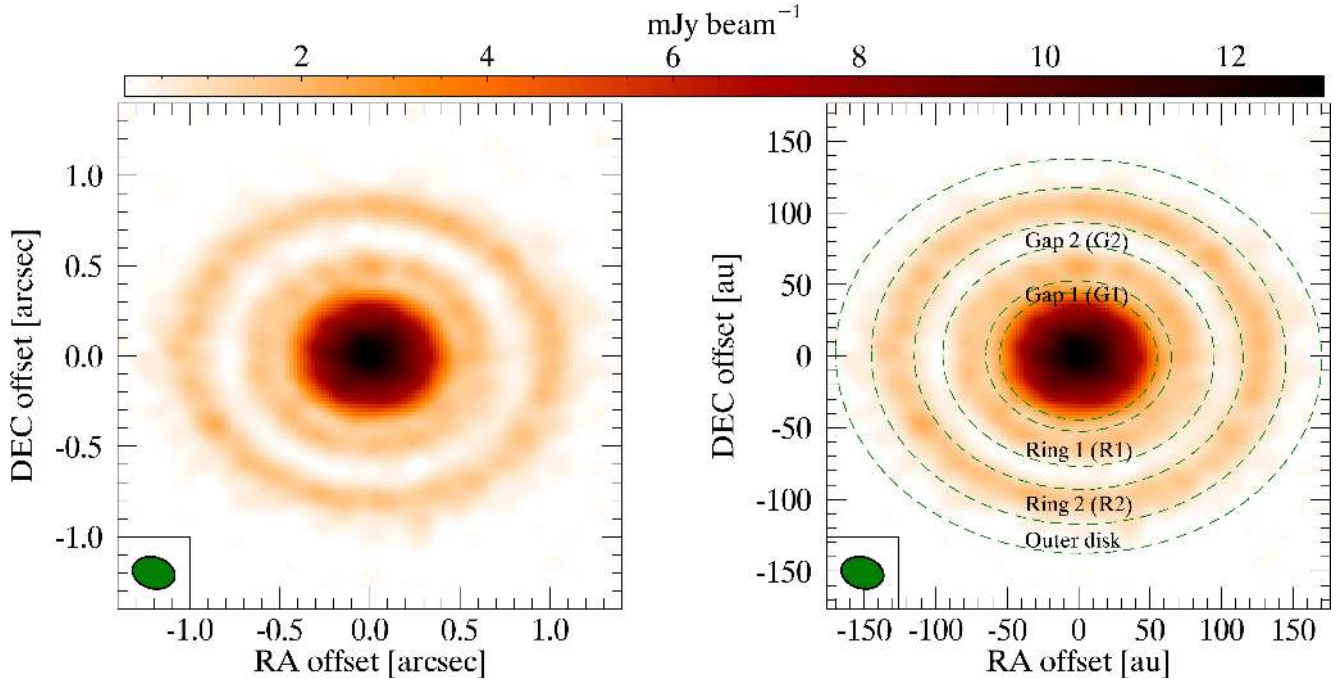
Fig. 1. ALMA 1.3 mm dust continuum image (uniform weighting). The main substructures are highlighted in the *right panel*.

The structure of the paper is the following: observations and data reduction are presented in Sect. 2 and the results are discussed in Sect. 3. The data analysis is described in Sect. 4. Section 5 provides a comparison to hydrodynamical simulations. Discussion and conclusion are reported in Sect. 6.

2. Observations and data reduction

The ALMA observations of AS 209 (J2000: RA = $16^h49^m15.296^s$, Dec = $-14°22'09.02''$) have been performed on 2016 September 22 (with 38 antennas) and 26 (41 antennas) in band 6 (211–275 GHz) as part of the project ID 2015.1.00486.S (PI: D. Fedele). The correlator setup includes a broad (2 GHz bandwidth) spectral window centered at 230 GHz.

Visibilities were taken in two execution blocks with a 6.05 s integration time per visibility totalling 40 min, per block, on-source. System temperatures were between 80–145 K. Weather conditions on the dates of observation gave an average precipitable water vapour of 2.2 and 2.3 mm, respectively. Calibration was done with J1517–2422 as bandpass calibrator, J1733–1304 as phase and flux the flux calibrator. The visibilities were subsequently time binned to 60 s integration times per visibility for self-calibration, imaging, and analysis. Self-calibration was performed using the 233 GHz continuum TDM spectral window with DA41 as the reference antenna.

The continuum image was created using CASA.CLEAN (CASA version 4.7); after trying different weighting schemes, we opted for a uniform weight which yields a synthesized beam of $0.''19 \times 0.''14$ (PA = 75.5°). The peak flux is 13 mJy beam^{-1} and the rms is 0.1 mJy beam^{-1}.

3. Results

The ALMA 1.3 mm dust continuum image is shown in Fig. 1: the continuum emission is characterized by a bright central emission

and two weaker dust rings peaking at ∼75 and 130 au, respectively. The two rings have a similar peak flux (∼2 mJy). The rings are intervaled by two narrow gaps. The two gaps have different widths and depths. The radial intensity profile shows a kink around 20–30 au which may be the signature of another (spatially unresolved) dust gap. Finally, the continuum flux does not drop to zero at the edge of the outer ring as there is a tenuous emission extending out to ∼170–180 au. The different disk substructures are clearly visible in the radial intensity profile shown in Fig. 2.

We fitted of the observed visibilities with the aim to provide an initial characterization of the disk surface brightness useful for the detailed physical modelling carried out in Sect. 4. We assumed an axisymmetric brightness profile defined as follows:

$$I(R) = \delta(R) \, I_0 \left(\frac{R}{R_c}\right)^{\phi_1} \exp\left[-\left(\frac{R}{R_c}\right)^{\phi_2}\right], \tag{1}$$

where I_0 is a normalization, R_c is a scale length and $\delta(R)$ is a scaling factor (by definition $\delta(R) > 0$) parametrized as:

$$\delta(R) = \begin{cases} \delta_{G1} & \text{for } R \in [R_{G1} - hw_{G1}, R_{G1} + hw_{G1}], \\ \delta_{R1} & \text{for } R \in [R_{G1} + hw_{G1}, R_{G2} - hw_{G2}], \\ \delta_{G2} & \text{for } R \in [R_{G2} - hw_{G2}, R_{G2} + hw_{G2}], \\ \delta_{R2} & \text{for } R \in [R_{G2} + hw_{G2}, R_{R2,\text{out}}], \\ \delta_{\text{out}} & \text{for } R \geq R_{R2,\text{out}}, \\ 1 & \text{otherwise}, \end{cases} \tag{2}$$

where R_G and hw_G are the center and half width of the dust gaps, respectively. The choice of this particular brightness profile serves as a simple realization of an "unperturbed" profile (an exponentially tapered power law), characterized by a few radial regions that can depart from it either due to an excess ($\delta > 1$) or a lack ($\delta < 1$) of emission. Following the evidence emerging from the synthesized image (Fig. 1), we allowed for two rings, two gaps, and an outer disk region, following nomenclature in Fig. 1. In this framework, a gap in the disk is naturally modelled with $\delta < 1$.
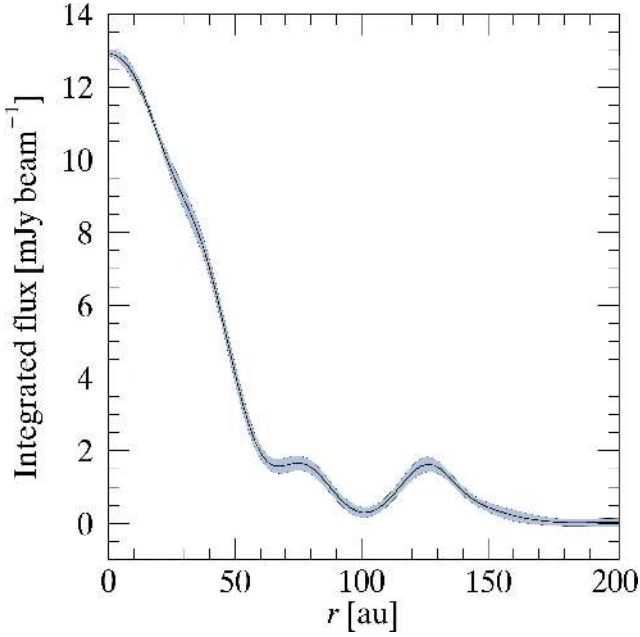
Fig. 2. Radial intensity profile of the 1.3 mm dust continuum emission. The profile is azimuthally averaged after deprojecting for the disk inclination ($i = 36°$, Sect. 3). The black line shows the mean profile while the shadowed regions indicate the standard deviation along the azimuth angle.

Table 1. Parameter space explored by the Markov chains and best-fit values.

Parameter	Min	Max	Best-fit
I_0 [mJy/beam]	0	100	7.4 ± 0.2
R_c [au]	20	150	80 ± 1
ϕ_1	-4	4	-0.24 ± 0.01
ϕ_2	-4	4	2.19 ± 0.02
R_{G1} [au]	0	80	61.7 ± 0.5
hw_{G1} [au]	0	30	8.0 ± 0.2
δ_{G1}	0	1	0.03 ± 0.005
δ_{R1}	0	3	0.80 ± 0.02
R_{G2} [au]	80	110	103.2 ± 0.4
hw_{G2} [au]	0	30	15.6 ± 0.2
δ_{G2}	0	1	0.025 ± 0.005
δ_{R2}	0	20	4.8 ± 0.1
$R_{R2,out}$ [au]	130	180	139.8 ± 0.8
δ_{out}	0	2	1.95 ± 0.03
i [°]	0	90	35.3 ± 0.8
PA [°]	0	180	86.0 ± 0.7

We performed the fit of the visibilities with a Bayesian approach using the Monte Carlo Markov chains (MCMCs) ensemble sampler (Goodman & Weare 2010) implemented in the EMCEE package (Foreman-Mackey et al. 2013). We assumed flat priors for all the free parameters. Table 1 reports the ranges explored for each parameter.

We also fitted simultaneously for the disk inclination i, the east-of-north position angle PA, and phase center offset ($\Delta\alpha$, $\Delta\delta$). For each set of values of the free parameters we compute a synthetic image of the model assuming axisymmetry and we use the GALARIO library (Tazzari et al. 2017) to compute the synthetic visibilities (by sampling the Fourier transform of the
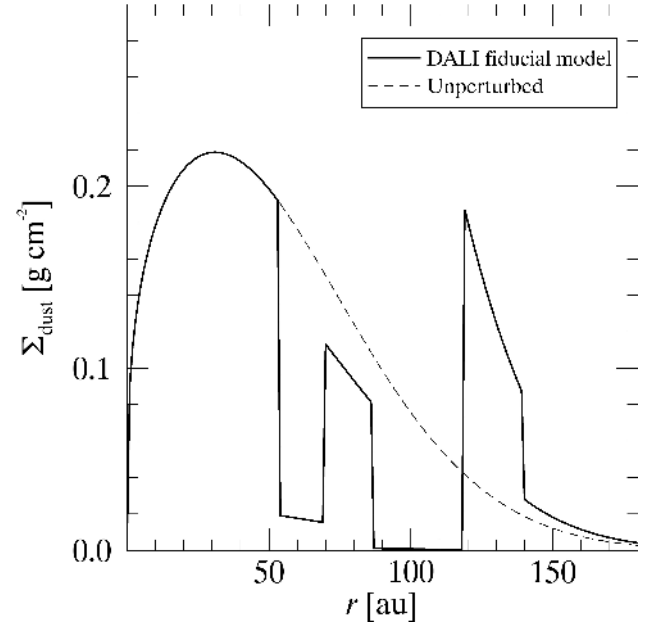
Fig. 3. Dust surface density of the DALI fiducial model. The dashed line corresponds to the initial unperturbed profile (power-law with exponential tail).

model image in all the observed (u, v)-points) and the resulting χ^2 as

$$\chi^2 = \sum_{j=0}^{N} |V_{obs}(u_j, v_j) - V_{mod}(u_j, v_j)|^2 w_j, \tag{3}$$

where w_j is the weight of the observed (u_j, v_j) visibility point. The posterior of each model is then computed as $\exp(-\chi^2/2)$ and sampled with 80 chains for 45 000 steps (after 5000 burn-in steps). The chains, which reached a good convergence, are shown in Fig. A.2, in the form of marginalized 1D and 2D distributions. The parameters that we infer from the fit of the visibilities are presented in Table 1: for each parameter, we estimate its value as the median of the marginalized distribution and its uncertainty as half the interval between 16% and 84% percentiles.

We find that the 1.3 mm continuum brightness distribution of AS 209 can be explained very well by a profile with two deep gaps ($\delta_{G1} \sim 0.03$, $\delta_{G2} \sim 0.025$) at 62 and 103 au, respectively, and an excess ring ($\delta_{R2} \sim 4$) at ~130 au. The excellent agreement of this profile with the observations is apparent in Fig. A.1, where the deprojected synthetic visibilities match the observed ones up to 1500 kλ.

4. Analysis with a physical disk model

In this section we aim to characterize the structure of AS 209 in physical terms, starting from the observed 1.3 mm continuum observation. This step is important to estimate the drop of the dust surface density inside the two gaps. For this purpose we use the dust radiative transfer code implemented into the thermo-chemical disk model DALI (Dust And LInes, Bruderer et al. 2012; Bruderer 2013). Starting from an input radiation field and from a disk density structure, DALI solves the two dimensional dust continuum radiative transfer and determines the dust temperature and radiation field strength at each disk position.

Table 2. DALI fiducial disk model.

Fixed parameter	Value	Description
$M_\star$ [$M_\odot$]	0.9[†]	Stellar mass
T_{eff} [K]	4250[†]	Stellar temperature
$L_\star$ [$L_\odot$]	1.5[†]	Stellar luminosity
d [pc]	126	Stellar distance
R_{in} [au]	0.1	Disk inner radius
R_c [au]	80	Disk critical radius
R_{G1} [au]	62	Gap 1 center
hw_{G1} [au]	8	Gap 1 half width
R_{G2} [au]	103	Gap 2 center
hw_G [au]	16	Gap 2 half width
$R_{R2,out}$ [au]	140	Ring 2 outer radius
R_{out} [au]	200	Disk outer radius
i [°]	35	Disk inclination
PA [°]	86	Disk position angle
χ, f_{large}	0.2, 0.85	Settling parameters
ψ	0.1[†]	Flaring exponent
h_c	0.133[†]	Scale height at R_c

Variable parameter	Min	Max	Step	Fiducial	
M_{dust} [$M_\odot$]	1×10^{-4}	5×10^{-4}	0.5×10^{-4}	3.5×10^{-4}	Disk dust mass
γ_1	-1.0	1.0	0.1	0.3	$\Sigma(r)$ power-law exponent
γ_2	1.0	3.0	0.1	2.0	$\Sigma(r)$ exponential-tail exponent
$\tilde{\delta}_{G1}$	(0, 0.001, 0.01, 0.05, 0.10, 0.15, 0.20)			0.1	$\Sigma_{dust,large}$ scale factor in gap 1
$\tilde{\delta}_{R1}$	0.5	1.0	0.05	0.75	$\Sigma_{dust,large}$ scale factor in ring 1
$\tilde{\delta}_{G2}$	(0, 0.001, 0.01, 0.02, 0.03, 0.05, 0.1)			0.01	$\Sigma_{dust,large}$ scale factor in gap 2
$\tilde{\delta}_{R2}$	2	5	0.5	4.5	$\Sigma_{dust,large}$ scale factor in ring 2
$\tilde{\delta}_{out}$	1	3	0.5	1.5	$\Sigma_{dust,large}$ scale factor in outer disk

Notes. For each variable parameter we explored a range of values between a minimum (Min) and maximum (Max) in regular steps (step). In the case of $\tilde{\delta}_{G1}$ and $\tilde{\delta}_{G2}$ we explored non-linearly spaced values, so we list them in parenthesis.
References. [†] Andrews et al. (2009).

4.1. Model description

We adopted the characterization of the surface brightness presented in the previous section as a first guess for the functional form and the location of the gaps to be used for the surface density of the physical disk model that we use in this section. The dust surface density is

$$\Sigma_{dust}(R) = \tilde{\delta}(R)\, \Sigma_c \left(\frac{R}{R_c}\right)^{\gamma_1} \exp\left[-\left(\frac{R}{R_c}\right)^{\gamma_2}\right], \quad (4)$$

where the surface density scaling factor ($\tilde{\delta}$) is parametrized as in Eq. (2).

In the vertical direction, the density follows a Gaussian distribution with scale height h ($= H/R$)

$$h = h_c \left(\frac{R}{R_c}\right)^{\psi}, \quad (5)$$

with h_c the critical scale height and ψ the flaring exponent. The critical scale height ($h_c = 0.13$) and disk flaring ($\psi = 0.1$) are taken from Andrews et al. (2011). In the adopted version of DALI, dust settling is included following D'Alessio et al. (2006), that is, adopting two power-law grain size populations with different scale heights: the small grains have a scale height equal to

h (similar to the gas) while the scale height of the large grains is χh (with $\chi < 1$) to account for the settling of the large grains. Finally, the total dust mass is distributed between the two populations and it is regulated by the parameter f_{large} (large-to-small mass ratio): thus, the dust surface density is $\Sigma_{dust} \cdot (1 - f_{large})$ and $\Sigma_{dust} \cdot f_{large}$ for the small and large grains, respectively. The flaring parameters are fixed : $\chi = 0.2$, $f_{large} = 0.85$.

We fixed the grain size populations with a small population of sizes between 0.005 and 1 μm and a large one of sizes between 0.005 μm and s_{max} with both populations sharing the same power-law exponent ($p = 3.5$). The dust mass absorption coefficients are taken from Andrews et al. (2011).

The maximum grain size of the large dust population affects the dust opacity at millimeter wavelengths with the opacity decreasing by almost an order of magnitude going from $s_{max} = 0.8$ mm to 1.0 cm (e.g., Tazzari et al. 2016). This in turn has an impact the dust temperature and the total dust mass. In this paper we fix $s_{max} = 2000$ μm in agreement with the multi-frequency continuum analysis of AS 209 by Tazzari et al. (2016).

4.2. Fiducial model

We built a grid of DALI disk models varying the following parameters: the total dust mass, the surface density power-law exponent (γ_1), the exponential tail exponent (γ_2) and the dust
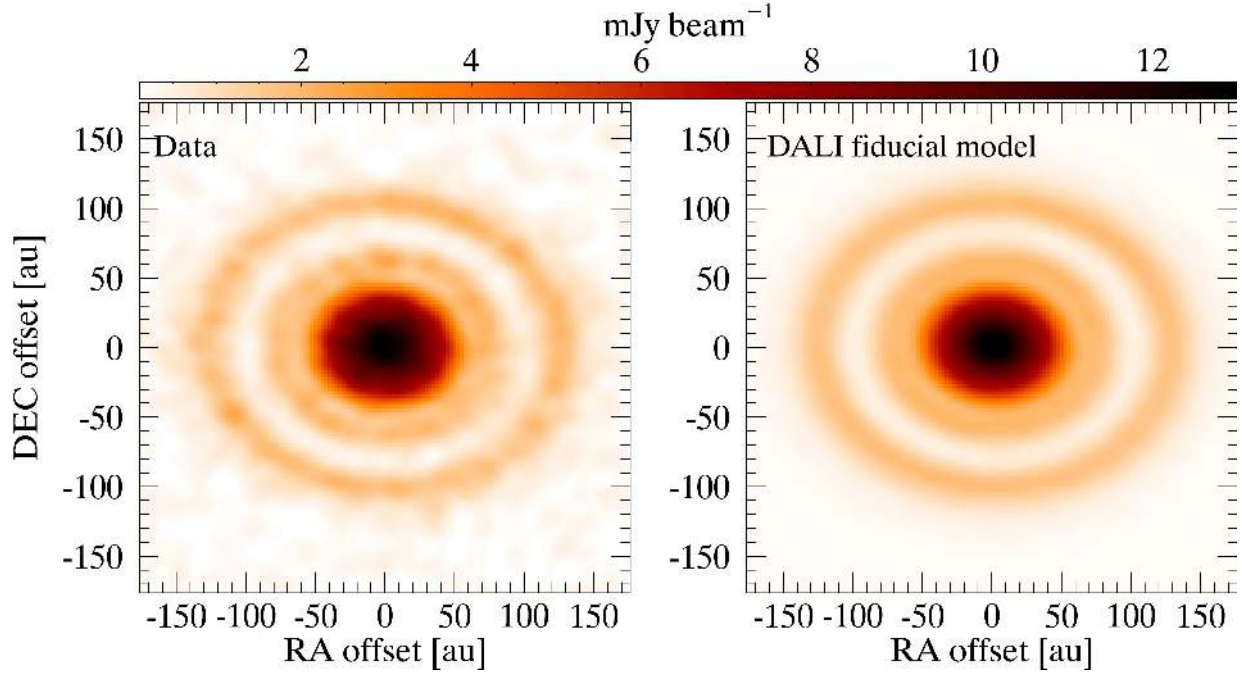
Fig. 4. DALI fiducial model, comparison of 1.3 mm continuum image. The model image is produced with CASA.CLEAN starting from the synthetic visibilities and adopting the same clean parameters as the observations.

density scaling factors. The explored range of each variable parameter is listed in Table 2. The values of R_c, gaps centers (R_{G1}, R_{G2}) and gaps sizes (half width hw_{G1}, hw_{G2}) are taken from the best-fist results of the multi-components analysis.

Each model was compared with the ALMA continuum observation with the aim of defining a fiducial model for the dust surface density. The comparison was performed in the uv-plane: first we computed the synthetic 1.3 mm continuum image with DALI, then the tool CASA.SIMOBSERVE is used to convert the image into synthetic visibilities at the same uv-positions as the observations. Finally we measured the χ^2 between observation and model after deprojecting and binning the visibilities (bin size of 30 kλ).

The fitting procedure was performed in multiple steps: first we varied the global disk properties, i.e. $M_{dust}, \gamma_1, \gamma_2$ until we find a good agreement with the visibilities at the shortest baselines which provides a constraint to the large scale structure. During this step the dust scaling factors are kept fixed: $\tilde{\delta}_{G1} = 0$, $\tilde{\delta}_{G2} = 0, \tilde{\delta}_{R1} = 1, \tilde{\delta}_{R2} = 1, \tilde{\delta}_{out} = 1$. In a second step, we constrained the values of the scaling factors while keeping fixed $M_{dust}, \gamma_1, \gamma_2$. The process was repeated until convergence. This allows us to refine the grid resolution iteratively.

The fiducial model is defined by the set of parameters that minimize the χ^2 between the observed and synthetic visibilities (Eq. (3)) within the explored parameter space.

The parameters of the DALI fiducial model are listed in Table 2. Figure 3 shows the dust surface density of the fiducial model and the model image is shown in Fig. 4. We note that, in order to quantitatively reproduce the disk structure (gaps and rings) with DALI we need to set different dust scaling factors for the two gaps: $\tilde{\delta}_{G1} \sim 0.1$ and $\tilde{\delta}_{G2} \sim 0.01$.
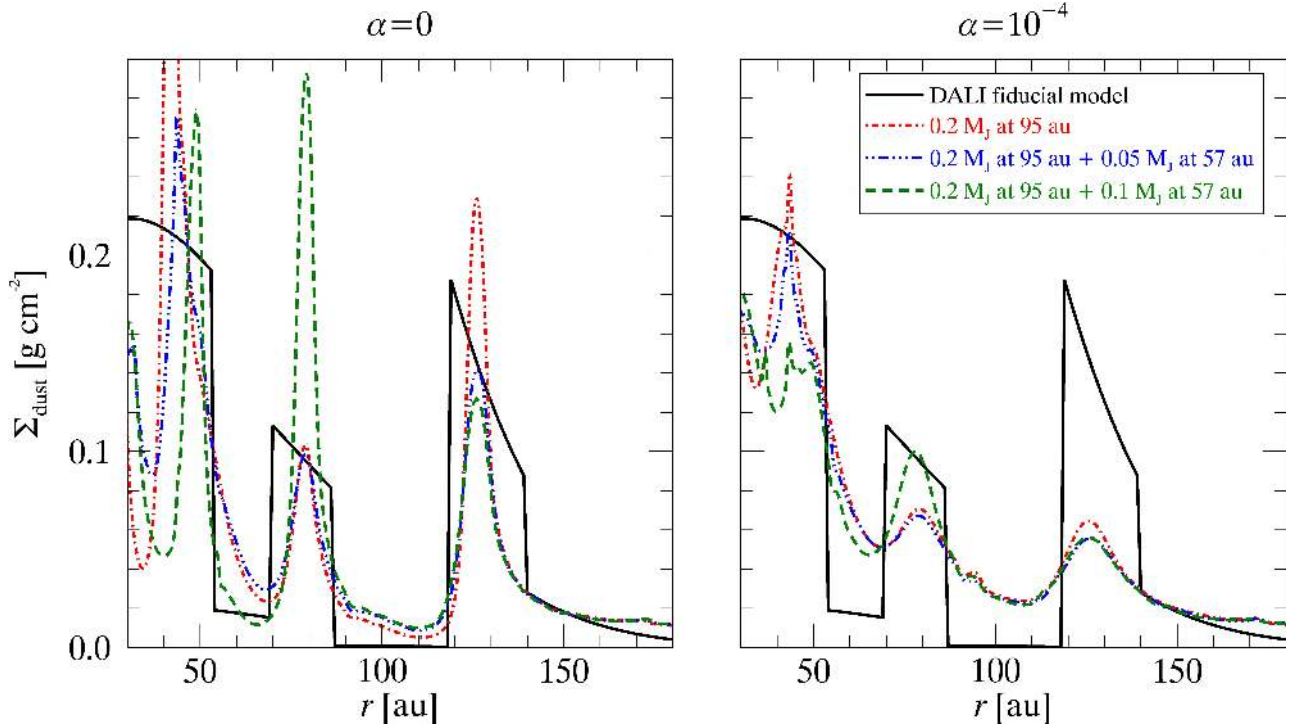
5. Comparison to hydrodynamical simulations

In this section we investigate the possibility that the gaps were produced by planets, as has been suggested for other disks,

for example HL Tau, TW Hydra, HD 163296, and HD 169142 (ALMA Partnership et al. 2015; Andrews et al. 2016; Isella et al. 2016; Fedele et al. 2017). To do this, we have run 2D simulations of planet-disk interaction using a version of FARGO-3D (Benítez-Llambay & Masset 2016) modified to include dust dynamics (Rosotti et al. 2016). The disk parameters were chosen to match the best fit model (see Table 3). The simulations were run using a logarithmic radial grid, extending from 10 to 300 au at a resolution of $Nr \times N\phi = 550 \times 1024$. Given the relative expense of the hydrodynamic simulations, we have not conducted an exhaustive fit to the data, instead we investigate the typical planetary properties and disk conditions that produce reasonable gap structures. The key information available for constraining the planets properties are the gap width, depth and location. The position of the two gap centers (62 and 103 au) are close enough to the ratio of radii expected for two planets migrating together in 2:1 resonance (with semi-major axis ratio 0.63), which forms the starting point for our investigation.

Starting from the relationship between the width of a gap opened by a planet and its mass derived by Rosotti et al. (2016), we already see that the inner planet must be low mass due because the inner gap is narrow (just 16 au or approximately two to three pressure scale-heights). This suggests that the mass of the inner planet is in the Neptune mass regime ($\sim 15\ M_\oplus$, i.e. 0.05 M_J). However, while Rosotti et al. (2016) showed that these planets can produce observable features, they found gap depths much smaller than the inner gap in AS 209. Nonetheless, the depth of the gap is sensitive to disk viscosity, with planets opening deeper gaps in low viscosity disks (Crida et al. 2006; Zhu et al. 2013). Thus together with the gap width, the gap depth places constraints on both the planet mass and disk viscosity. Furthermore, at extremely low viscosity, Dong et al. (2017) and Bae et al. (2017) showed that planets may open multiple dust gaps in inviscid disks, which raises the interesting possibility that the gaps in AS 209 may be opened by a single planet.

From the right panel of Fig. 5, we see that even a modest viscosity $\alpha = 10^{-4}$ is too high to produce deep enough gaps to

Fig. 5. Results of hydrodynamical simulations for the inviscid (*left*) and $\alpha = 10^{-4}$ (*right*) case. The black line corresponds to the dust surface density determined with DALI (Sect. 4). The (red) dot-dashed line is the 1 mm grains surface density based on the single planet scenario with 0.2 M_J planet at 95 au after 0.65 Myr (Sect. 5). The (blue) dot-dot-dashed and the (green) dashed curves corresponds to the two planets scenario with an inner planet of mass 0.05 and 0.1 M_J, respectively.

explain the structures in AS 209. While a single 0.2 M_J planet at 95 au matches the width of the outer gap, the drop in dust surface density it is far too shallow compared to what is inferred. Although more massive planets can open deep enough gaps (for $\alpha = 10^{-4}$), they produce structures that are too wide and begin to prevent the inflow of dust entirely. This suggests that the outer gap is consistent with a 0.2 M_J planet, but requires even lower viscosity. The planet was injected at $t = 0$ and the simulation was stopped after 0.65 Myr.

The inviscid ($\alpha = 0$) simulations produce a much better match to the inferred gap structure (Fig. 5, left panel). Already a single 0.2 M_J planet at 95 au is in remarkable agreement with the gap structure, producing a deep outer gap along with a second inner gap at approximately the right location and with a reasonable width and depth. The depth of the gaps is not only sensitive to viscosity, but in the inviscid case it also increases with time, thus being a much weaker tracer of the planet mass than the position of the peaks (as noted by Rosotti et al. 2016). However, the width of the gaps are similar in both the viscous and inviscid cases. Interestingly, the simulations produce an additional gap at around 35 au, which coincides with similar, but much smaller amplitude, feature in the radial intensity profile (Fig. 2). Given that the depth of this feature is dependent on parameters such as viscosity, and optical depth effects may further reduce the amplitude of variation in the observed intensity profile, it is possible that this inner structure is related to the presence of a planet near 100 au.

Since low viscosity is required to reproduce the gap structure in AS 209, and in this case a single planet may produce both gaps, it is interesting to consider whether there still could be a second planet present. Thus we have re-run both the viscous and inviscid simulations with an inner planets at 57 au, close to the 2:1 resonance with the outer planet. In both cases the planet mass

Table 3. Disk model used in the planet disk-interaction simulations.

Parameter	Value
Temperature	$190(R/100 \text{ au})^{-0.55}$
Gas surface density	$7.5(R/100 \text{ au})^{-1}$
Grain size	1 mm
Viscous α	0, 10^{-4}

is consistent with the estimate from the relationship between gap width and planet mass: a 0.05 M_J planet produces a negligible difference to the structure of the gaps and could thus be easily hidden in the gap. The largest planet mass compatible with the gap widths is roughly 0.1 M_J, with larger planet masses producing a gap that is too wide in the inviscid case. While a slightly more massive planet may be compatible with the inner gap when $\alpha = 10^{-4}$, this is hard to reconcile with the need for a lower α in the outer gap.

6. Conclusions

The ringed dust structure of AS 209 revealed by ALMA is consistent with the presence of a Saturn-like ($M_{planet} = 0.2 M_J = 0.67 M_{Saturn}$) planet at $r = 95$ au. The planetary mass is constrained by the width and depth of the dust gap: for the chosen gas properties, our hydrodynamical simulations indicate that less massive planets ($\lesssim 0.5 M_{Saturn}$) do not produce a gap that is sufficiently wide, while more massive planets ($\gtrsim 1.0 M_{Saturn}$) prevent the transport of dust inwards entirely, forming a transition disk (inner hole in large grains). Our radiative transfer calculations (Sect. 4) show that surface density of the mm grains beyond

the planet orbit is enhanced and largely confined in a narrow ring. This may be the signature of dust pile-up due to the planet-induced gas pressure maximum beyond the orbit of the planet. Interestingly, the ALMA $C^{18}O$ image presented in Huang et al. (2016) shows an extended emission peaking at nearly 130 au. This extended emission is co-spatial to the outer dust ring. This is a strong indication that the large scale $C^{18}O$ emission follows the actual disk surface density in the outer disk and it points to a gas density drop by a factor of a few inside the outer gap ("G2").

We have also investigated the existence of a second planet in correspondence of the inner dust gap. We conclude that there could be a second planet present in the inner gap if it is less than about 0.1 M_J. Since the two gaps are close to the 2:1 resonance this raises the possibility that the structure could be caused by a pair of planets migrating in resonance. The 1 mm surface density resulting from a pair of 0.05 M_J–0.2 M_J is in remarkable agreement with the observations. Nonetheless, while both scenarios require low disk turbulence, the presence of the inner planet is not needed to explain the observed structures.

The inferred presence of the Saturn-like planet at $r \sim 95$ au raises new questions about planet formation at such large distance from the star. Gravitational instability can occur on short timescales and is a viable process for the formation of giant planets on wide orbits (e.g., Kratter & Lodato 2016). An alternative scenario is pebble accretion, in which planets grow through the accretion of cm-sized (or larger) grains that are weakly coupled to the gas (Lambrechts & Johansen 2012). In this case however planet formation is challenged by dust migration: according to dust evolution models such large dust grains are expected to drift towards the star in much less than a Myr (e.g., Takeuchi et al. 2005; Brauer et al. 2008), which is difficult to reconcile with disk lifetimes (a few Myr, e.g., Fedele et al. 2010).

In the case of AS 209, the dust inward migration is likely to be slowed down by the presence of radial dust traps induced by the presence of a Saturn-like planet. While this can help to reconcile the presence of large dust with the disk's lifetime, it must hinder pebble accretion in the inner disk, restricting this mode of planet formation to the earliest phases of disk evolution, on timescales $\lesssim 1$ Myr.

References

ALMA Partnership, Brogan, C. L., Pérez, L. M., et al. 2015, ApJ, 808, L3
Andrews, S. M., Wilner, D. J., Hughes, A. M., Qi, C., & Dullemond, C. P. 2009, ApJ, 700, 1502
Andrews, S. M., Wilner, D. J., Espaillat, C., et al. 2011, ApJ, 732, 42
Andrews, S. M., Wilner, D. J., Zhu, Z., et al. 2016, ApJ, 820, L40
Bae, J., Zhu, Z., & Hartmann, L. 2017, ApJ, 850, 201B
Benítez-Llambay, P., & Masset, F. S. 2016, ApJS, 223, 11
Birnstiel, T., Klahr, H., & Ercolano, B. 2012, A&A, 539, A148
Brauer, F., Dullemond, C. P., & Henning, T. 2008, A&A, 480, 859
Bruderer, S. 2013, A&A, 559, A46
Bruderer, S., van Dishoeck, E. F., Doty, S. D., & Herczeg, G. J. 2012, A&A, 541, A91
Crida, A., Morbidelli, A., & Masset, F. 2006, Icarus, 181, 587
D'Alessio, P., Calvet, N., Hartmann, L., Franco-Hernández, R., & Servín, H. 2006, ApJ, 638, 314
Dong, R., Li, S., Chiang, E., & Li, H. 2017, ApJ, 843, 127
Ercolano, B., Rosotti, G. P., Picogna, G., & Testi, L. 2017, MNRAS, 464, L95
Fedele, D., van den Ancker, M. E., Henning, T., Jayawardhana, R., & Oliveira, J. M. 2010, A&A, 510, A72
Fedele, D., Carney, M., Hogerheijde, M. R., et al. 2017, A&A, 600, A72
Flock, M., Ruge, J. P., Dzyurkevich, N., et al. 2015, A&A, 574, A68
Foreman-Mackey, D., Hogg, D. W., Lang, D., & Goodman, J. 2013, PASP, 125, 306
Gaia Collaboration (Brown, A. G. A., et al.) 2016, A&A, 595, A2
Goodman, J., & Weare, J. 2010, Commun. Appl. Math. Comput. Sci., 5, 65
Huang, J., Öberg, K. I., & Andrews, S. M. 2016, ApJ, 823, L18
Huang, J., Öberg, K. I., & Qi, C., et al. 2017, ApJ, 835, 231
Isella, A., Guidi, G., & Testi, L., et al. 2016, Phys. Rev. Lett., 117, 251101
Kratter, K., & Lodato, G. 2016, ARA&A, 54, 271
Lambrechts, M., & Johansen, A. 2012, A&A, 544, A32
Loomis, R. A., Öberg, K. I., Andrews, S. M., & MacGregor, M. A. 2017, ApJ, 840, 23
Natta, A., Testi, L., & Randich, S. 2006, A&A, 452, 245
Okuzumi, S., Momose, M., Sirono, S.-i., Kobayashi, H., & Tanaka, H. 2016, ApJ, 821, 82
Papaloizou, J., & Lin, D. N. C. 1984, ApJ, 285, 818
Pérez, L. M., Carpenter, J. M., Chandler, C. J., et al. 2012, ApJ, 760, L17
Pinilla, P., Birnstiel, T., Ricci, L., et al. 2012, A&A, 538, A114
Rosotti, G. P., Juhasz, A., Booth, R. A., & Clarke, C. J. 2016, MNRAS, 459, 2790
Takeuchi, T., Clarke, C. J., & Lin, D. N. C. 2005, ApJ, 627, 286
Tazzari, M., Testi, L., Ercolano, B., et al. 2016, A&A, 588, A53
Tazzari, M., Beaujean, F., & Testi, L. 2017, MNRAS, submitted, [arXiv:1709.06999]
Zhang, K., Blake, G. A., & Bergin, E. A. 2015, ApJ, 806, L7
Zhu, Z., Stone, J. M., & Rafikov, R. R. 2013, ApJ, 768, 143

Appendix A: Monte Carlo Markov chain
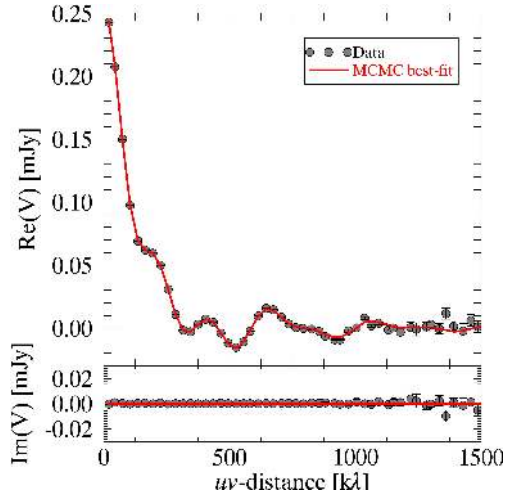
Fig. A.1. Results of multi-components geometrical fit with MCMC: comparison of the observed (gray dots) and bestfit model (red line) deprojected visibilities.
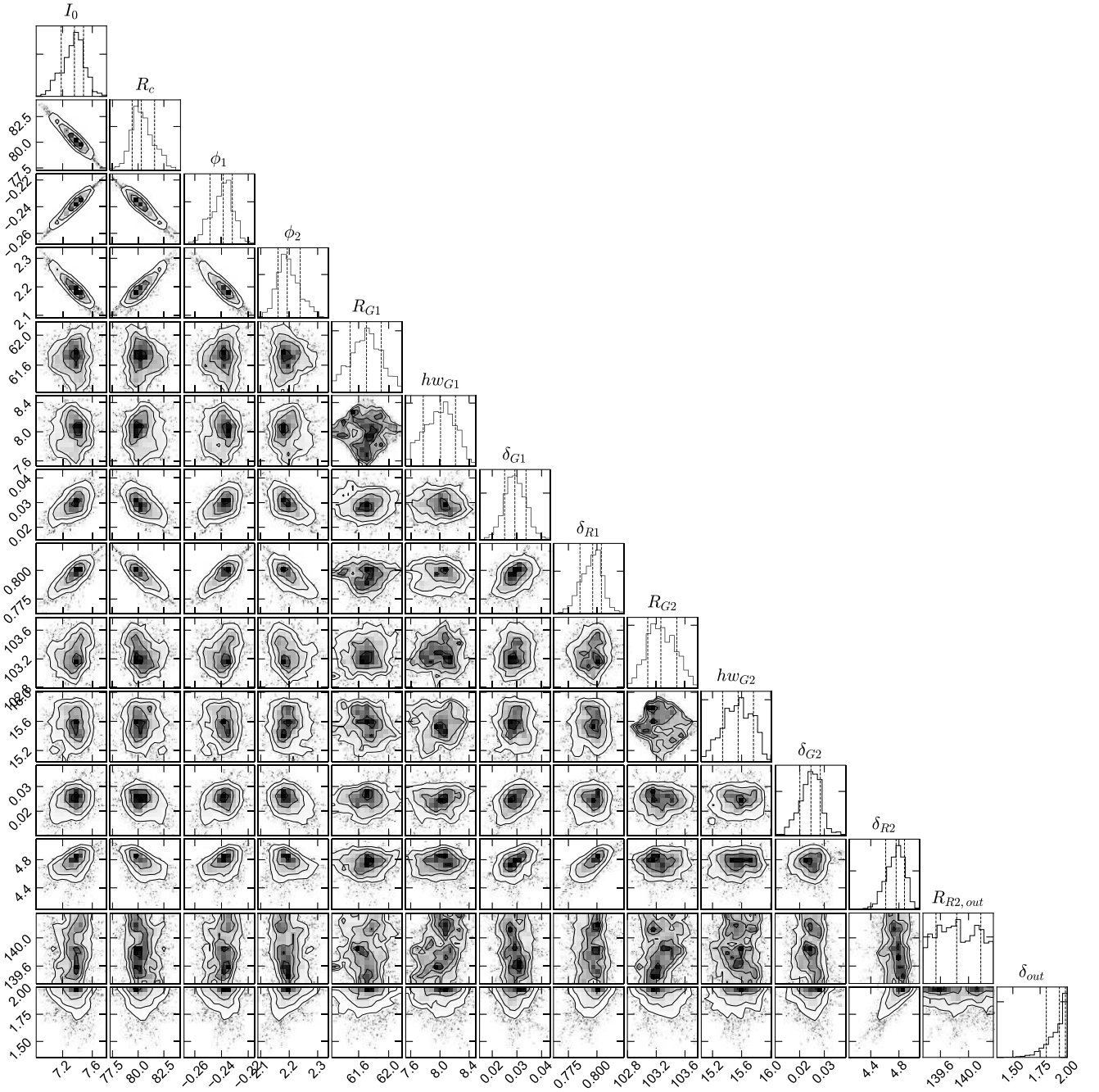
Fig. A.2. 1D and 2D marginalized distributions of the posterior sampling obtained from MCMC. In the 1D marginalized distributions of each parameter the vertical dashed lines represent the 16th, 50th and 84th percentiles: the median is taken as the bestfit value, and half the interval between 16th and 84th percentiles as the uncertainty.